

Appendix A. Supplementary data

Cu-Co bimetallic nanoclusters Mott-Schottky interaction increasing oxygen reduction reaction activity in rechargeable Zn-air battery

Qing Dong,^a Haoran Wang,^a Fangfang Liu,^b Jianwei Ren,^{*c} Hui Wang,^a Xuyun Wang,^a and Rongfang Wang^{*a}

^a *State Key Laboratory Base for Eco-Chemical Engineering, College of Chemical Engineering, Qingdao University of Science and Technology, Qingdao, 266042, China.*

^b *Weifang University of Science and Technology, Shouguang, Weifang, 262700, China*

^c *Department of Mechanical Engineering Science, University of Johannesburg, Cnr Kingsway and University Roads, Auckland Park, 2092, Johannesburg, South Africa.*

* Corresponding authors.

E-mail addresses: jren@uj.ac.za (J. Ren), rfwang@qust.edu.cn (R. Wang).

Physical characterization

The morphology of the as-prepared samples was studied by field-emission scanning electron microscopy (FESEM) on a Carl Zeiss Ultra Plus system. Transmission electron microscopy (TEM) images, high angle annular dark field scanning transmission electron microscopy (STEM) images and selected area electron diffraction (SAED) images of the catalysts were observed under JEOL (JEM-2000FX) microscope operating at 200 kV. Brunauer-Emmett-Teller (BET) was used to measure the specific surface area of all the prepared samples, and density functional theory (DFT) method was used to calculate the pore size distribution of carbon materials. X-ray diffraction

(XRD) patterns of the as-prepared samples were recorded on a Shimadzu XD-3A instrument using filtered Cu-K α radiation ($\lambda = 0.15418$ nm), generated at 40 kV and 30 mA. Scans for 2θ values were recorded at 5° min^{-1} between 10° and 90° . The X-ray photoelectron spectroscopy (XPS) was acquired with a VG ESCALAB210 spectrometer equipped with an MG 300 W X-ray source. Ultraviolet photoelectron spectroscopy (UPS) measurements were carried out by a Prevac spectrometer with a VG Scienta R3000 hemispherical electron energy analyzer. Photons with energy of 21.22 eV generated by helium I were used for UPS spectra. Fourier transform infrared (FT-IR) spectrometry was carried out using a FTIR-8400S spectrophotometer (Shimadzu, Japan).

Experimental Section

Oxygen electrocatalytic measurements

The oxygen reduction reaction (ORR) performance was evaluated in a conventional three-electrode cell on a WaveDriver 20 bipotentiostat (Pine Instrument Company, USA). A rotating disk electrode (RDE) with a glass carbon disk (5 mm in diameter), and a rotating ring-disk electrode (RRDE) with a Pt ring (6.5 mm in inner diameter and 8.5 mm in outer diameter) and a glass carbon disk (5.5 mm in diameter) coated with catalyst film were used as the working electrodes. Ag/AgCl in saturated KCl was chosen as a reference electrode and Pt wire (ORR) as a counter electrode. The working electrode was prepared as follows: 5 mg of catalyst were dispersed into 1 mL Nafion ethanol solution (0.25 wt.%) by ultrasonic mixing for 30 min. 8 mL of ink containing 40 mg catalyst were dropped onto the surface of a polished glass-carbon rotating disc

electrode (catalyst loading: 0.196 mg cm⁻²) and air dried. For performance comparison, commercial Pt/C (20 wt.% Johnson Matthey) catalysts were used for the preparation of working electrodes according to the same procedure. 0.1 M KOH purged with N₂ for 30 min was used as an electrolyte for all electrochemical tests in this study. All potential values recorded in the study were converted to potentials vs. reversible hydrogen electrode (RHE) using the following equation: $E_{RHE} = E_{Ag/AgCl} + 0.059 pH + 0.197 V$. iR curve compensation was done in the tests and ORR curves were adjusted to take capacitive effects into account. The durability testing of ORR was carried out by continuous cyclic voltammetry (CV) in the potential range of 0.036–1.164 V vs. RHE at a scan rate of 50 mV s⁻¹ in 0.1 M KOH electrolyte for 3000 and 6000 cycles. The apparent electron transfer number (n) was calculated based on the K-L equation:

$$\frac{1}{j} = \frac{1}{j_L} + \frac{1}{j_k} = \frac{1}{B\omega^{1/2}} + \frac{1}{j_K} \quad (1)$$

$$B = 0.62nFC_0D_0^{2/3}\nu^{-1/6} \quad (2)$$

where j is the measured current density, j_K and j_L are the kinetic and limiting current densities, respectively, ω is the angular velocity of the disk, n is the electron transfer number, F is the Faraday constant (96485 C mol⁻¹), C_0 is the bulk concentration of O₂ (1.2 × 10⁻³ mol L⁻¹), D_0 is the diffusion coefficient of O₂ (1.9 × 10⁻⁵ cm² s⁻¹), and ν is the kinematic viscosity of the electrolyte (0.01 cm² s⁻¹).

RRDE measurements were performed at the voltage range from 0.2 to 1.2 V versus RHE in O₂-saturated electrolyte at a rotation speed of 1600 rpm with a scan rate of 10 mV s⁻¹. The yield of H₂O₂ and the electron transfer number (n) could be determined by the following equations:

$$H_2O_2\% = 200 \frac{I_r/N}{I_d + I_r/N} \quad (3)$$

$$n = 4 \frac{I_d}{I_d + I_r/N} \quad (4)$$

where I_d is the disk current, I_r is the ring current, and N is the current collection efficiency of the Pt ring, which was 0.37, provided by the manufacturer.

The oxygen evolution reaction (OER) performance tests were carried out in a conventional three-electrode cell on a CHI760D electrochemical analyzer (CH Instruments). Oxygen evolution reaction (OER) was tested in 1.0 M KOH (pH = 13.6) in a three-electrode cell with a carbon rod as the counter electrode, a Hg/HgO as the reference electrode, and the catalyst as the working electrode. The working electrode was prepared as follows: 2.5 mg of catalyst were dispersed into 0.5 mL Nafion ethanol solution (0.40 wt.%) by ultrasonic mixing for 30 min. 0.2 mL of ink containing 1 mg catalyst were dropped onto the surface of nickel foam (NF) with a size of 1×1 cm (catalyst loading: 1 mg cm⁻²) and air dried. For performance comparison, the same loading of commercial RuO₂ (Johnson Matthey) catalysts were used for the preparation of working electrodes according to the same procedure. Electrochemical impedance spectroscopy (EIS) measurements were conducted on a CHI 660E electrochemical workstation in the range of 0.01 Hz to 100000 Hz with 5 mV sinusoidal perturbations. All the potentials and voltages were iR-corrected, calibrated, and converted to the RHE, according to $E_{RHE} = E_{Hg/HgO} + 0.059 \text{ pH} + 0.098 \text{ V}$.

Zn-air battery performance measurements

Liquid Zn-air battery (ZAB) were assembled and tested. The air cathode was

prepared by dispersing 4 mg of the catalyst, 3 μL of polymer binder PTFE, 4 mg of Vulcan carbon in 300 μL isopropyl alcohol to form a homogenous slurry. After rolling into a slice and oven drying at 40 $^{\circ}\text{C}$, the air cathode mixture was pressed onto Ni foam under 20 MPa. A polished zinc plate with a thickness of 0.5 mm and a width of 1 cm and 6 M KOH solution containing 0.2 M of $\text{Zn}(\text{OAc})_2$ were used as the anode and the electrolyte, respectively. The gas diffusion area is 1 cm^2 allowing O_2 access to the active sites of catalysts. For comparison, 2 mg of commercial Pt/C (20 wt.% Johnson Matthey) and 2 mg of commercial RuO_2 are mixed as catalysts to prepare Pt/C+ RuO_2 air cathode.

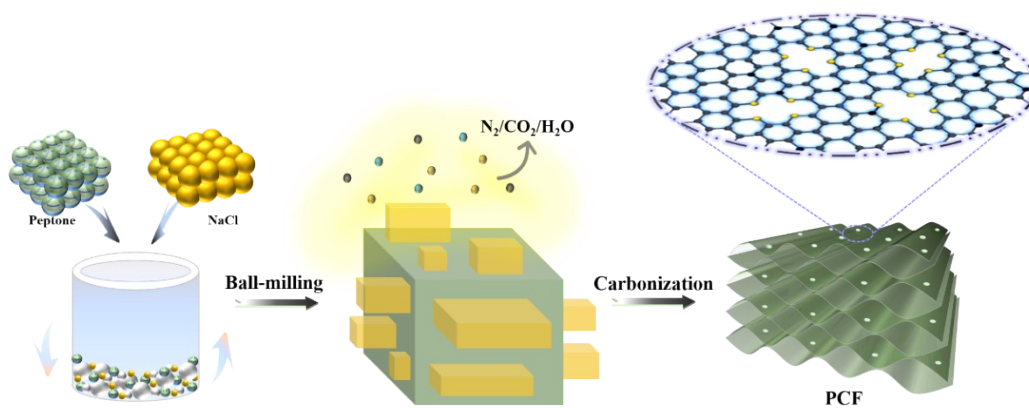


Fig. S1. Synthetic procedure of the PCF sample.

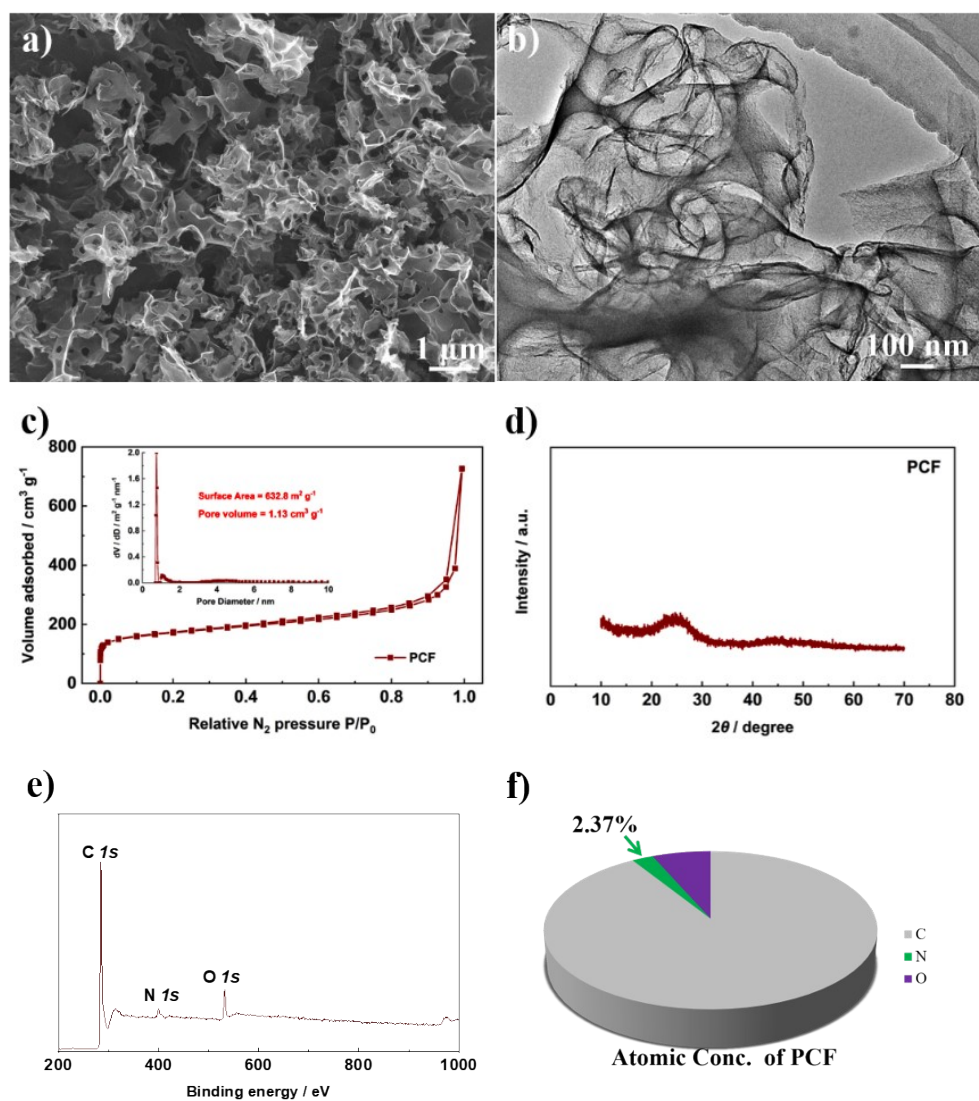


Fig. S2. (a) SEM image, (b) TEM image, (c) N_2 adsorption-desorption isotherms and pore-size-distributions, (d) XRD pattern, (e) XPS spectrum and (f) atomic conc. of PCF sample.

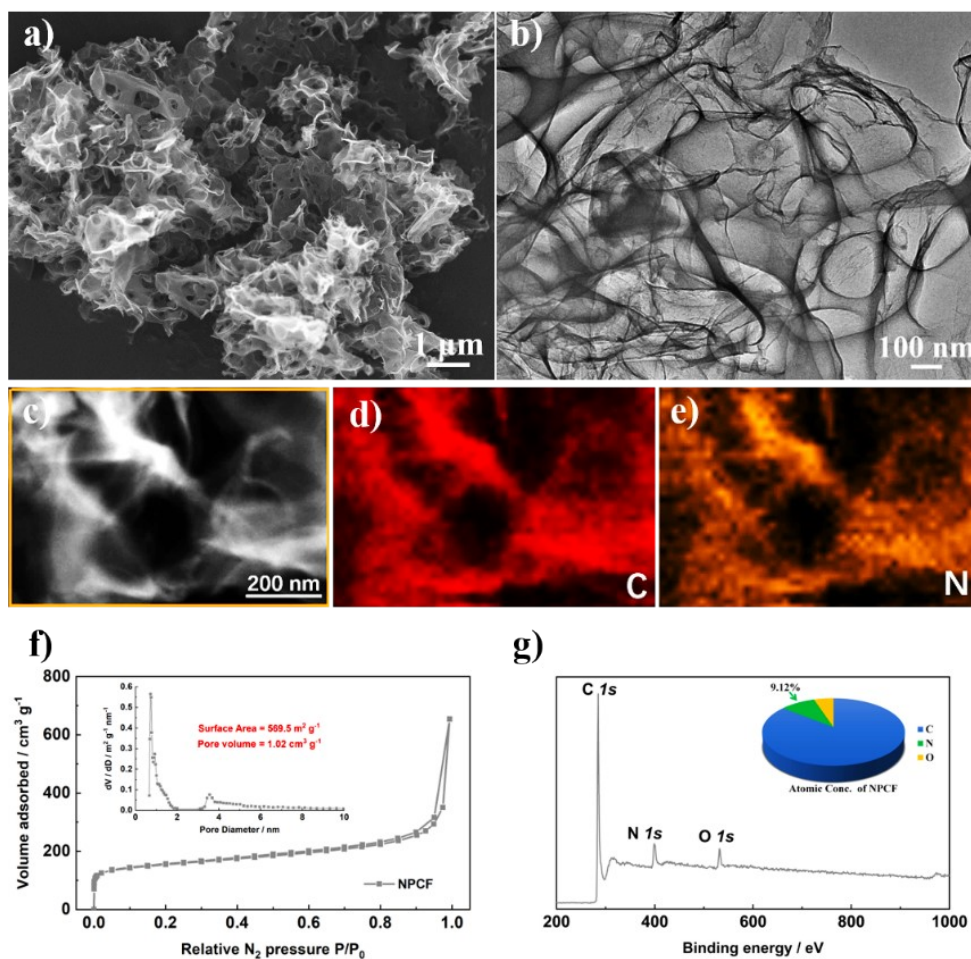


Fig. S3. (a) SEM image, (b) TEM image, (c) STEM image, Element mappings of (d) C, (e) N, (f) N_2 adsorption-desorption isotherms and pore-size-distributions, and (g) XPS spectrum of NPCF sample.

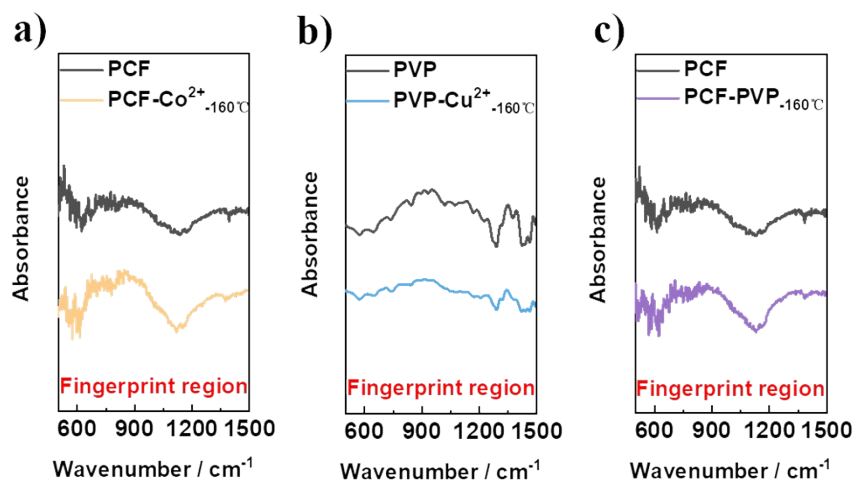


Fig. S4. (a) FTIR spectra of PCF and the as-prepared PCF- Co^{2+} -160°C samples. (b) FTIR spectra of PVP and the as-prepared PVP- Cu^{2+} -160°C samples. (c) FTIR spectra of PCF and the as-prepared PCF-PVP -160°C samples.

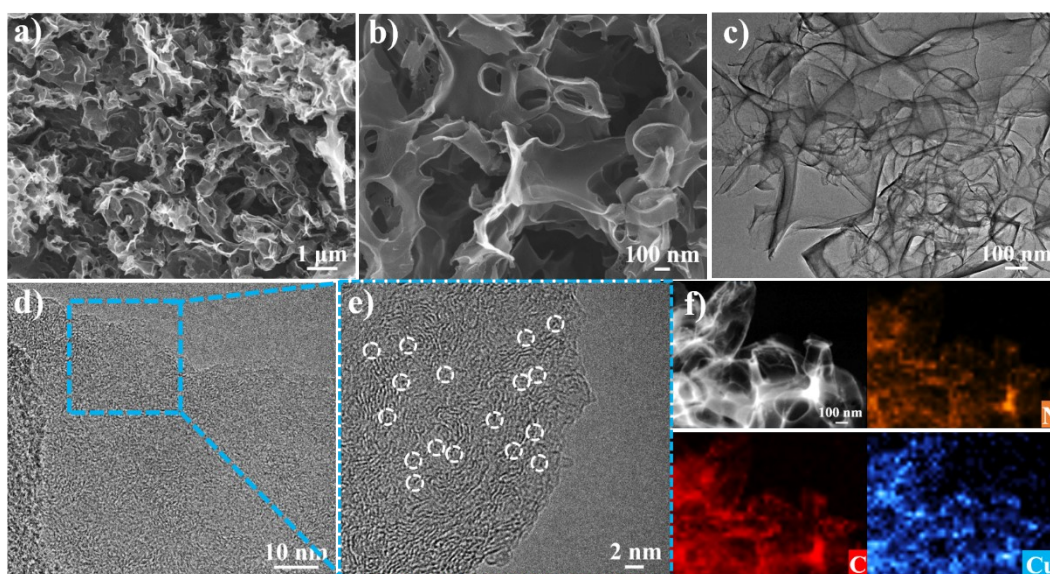


Fig. S5. (a-b) SEM image, (c) TEM image, (d-e) HRTEM images, (f) STEM image and corresponding element mappings of $\text{Cu}_{\text{NCs}}\text{-NPCF}$ sample.

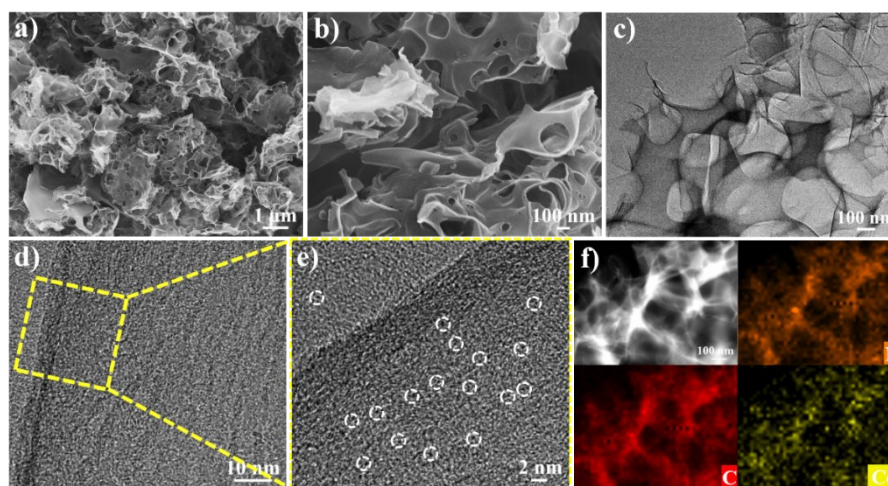


Fig. S6. (a-b) SEM image, (c) TEM image, (d-e) HRTEM images, (f) STEM image and corresponding element mappings of $\text{Co}_{\text{NCs}}\text{-NPCF}$ sample.

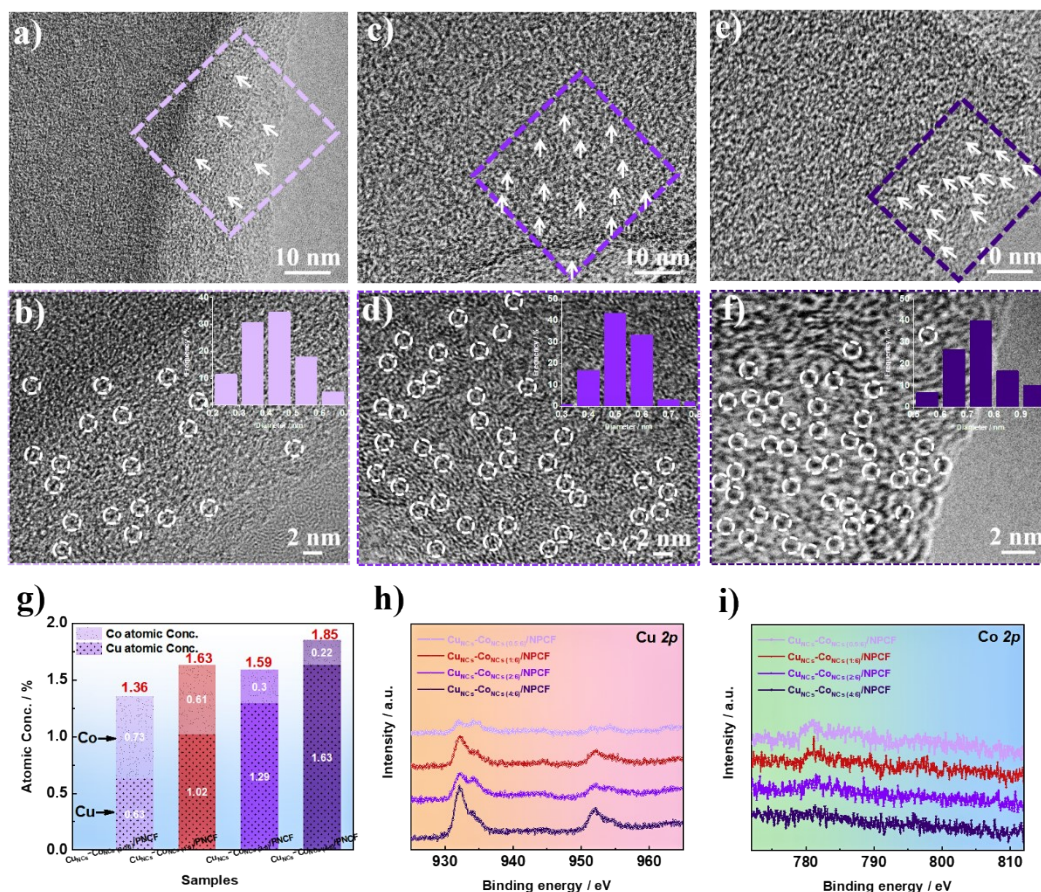


Fig. S7. (a-b) TEM image of $\text{Cu}_{\text{NCs}}-\text{Co}_{\text{NCs}}(0.5:6)/\text{NPCF}$. (c-d) TEM image of $\text{Cu}_{\text{NCs}}-\text{Co}_{\text{NCs}}(2:6)/\text{NPCF}$. (e-f) TEM image of $\text{Cu}_{\text{NCs}}-\text{Co}_{\text{NCs}}(4:6)/\text{NPCF}$. (g) Cu atomic concentration and Co atomic concentration within the $\text{Co}_{\text{NCs}}(0.5:6)/\text{NPCF}$, $\text{Cu}_{\text{NCs}}-\text{Co}_{\text{NCs}}(1:6)/\text{NPCF}$, $\text{Cu}_{\text{NCs}}-\text{Co}_{\text{NCs}}(2:6)/\text{NPCF}$ and $\text{Cu}_{\text{NCs}}-\text{Co}_{\text{NCs}}(4:6)/\text{NPCF}$ samples. (h) Cu 2p XPS spectrum and (i) Co 2p XPS spectra of $\text{Co}_{\text{NCs}}(0.5:6)/\text{NPCF}$, $\text{Cu}_{\text{NCs}}-\text{Co}_{\text{NCs}}(1:6)/\text{NPCF}$, $\text{Cu}_{\text{NCs}}-\text{Co}_{\text{NCs}}(2:6)/\text{NPCF}$ and $\text{Cu}_{\text{NCs}}-\text{Co}_{\text{NCs}}(4:6)/\text{NPCF}$ samples.

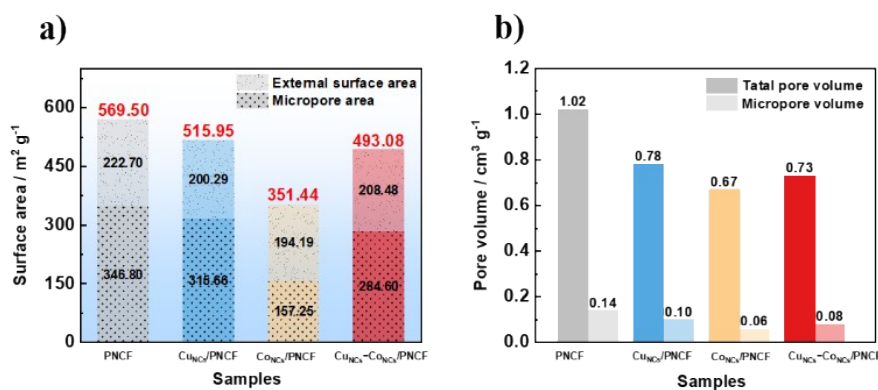


Fig. S8. (a) Surface area, external surface area and micropore area, and (b) Pore volumes of the NPCF, $\text{Cu}_{\text{NCs}}/\text{NPCF}$, $\text{Co}_{\text{NCs}}/\text{NPCF}$ and $\text{Cu}_{\text{NCs}}-\text{Co}_{\text{NCs}}/\text{NPCF}$ samples.

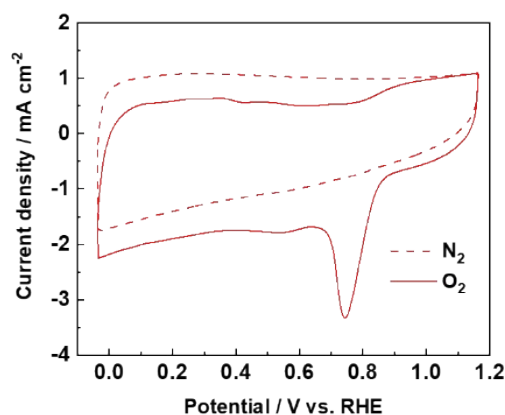


Fig. S9. CV profiles of the $\text{Cu}_{\text{NCS}}\text{-Co}_{\text{NCS}}/\text{NPCF}$ catalyst sample in O_2 - (red) and N_2 - (black) saturated 0.1 M KOH solution.

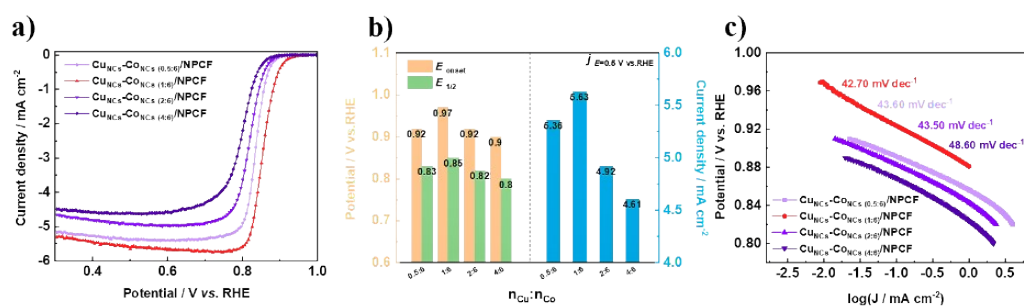


Fig. S10. (a) ORR linear scan voltammograms (LSV) at 1600 rpm in an O_2 -saturated 0.10 M KOH with a scan rate of 5 mV s^{-1} , (b) corresponding E_{onset} , $E_{1/2}$ and $J_{E=0.5 \text{ V vs. RHE}}$ values, (c) Tafel plots of $\text{Cu}_{\text{NCS}}\text{-Co}_{\text{NCS}} (0.5:6)/\text{NPCF}$, $\text{Cu}_{\text{NCS}}\text{-Co}_{\text{NCS}} (1:6)/\text{NPCF}$, $\text{Cu}_{\text{NCS}}\text{-Co}_{\text{NCS}} (2:6)/\text{NPCF}$ and $\text{Cu}_{\text{NCS}}\text{-Co}_{\text{NCS}} (4:6)/\text{NPCF}$ samples.

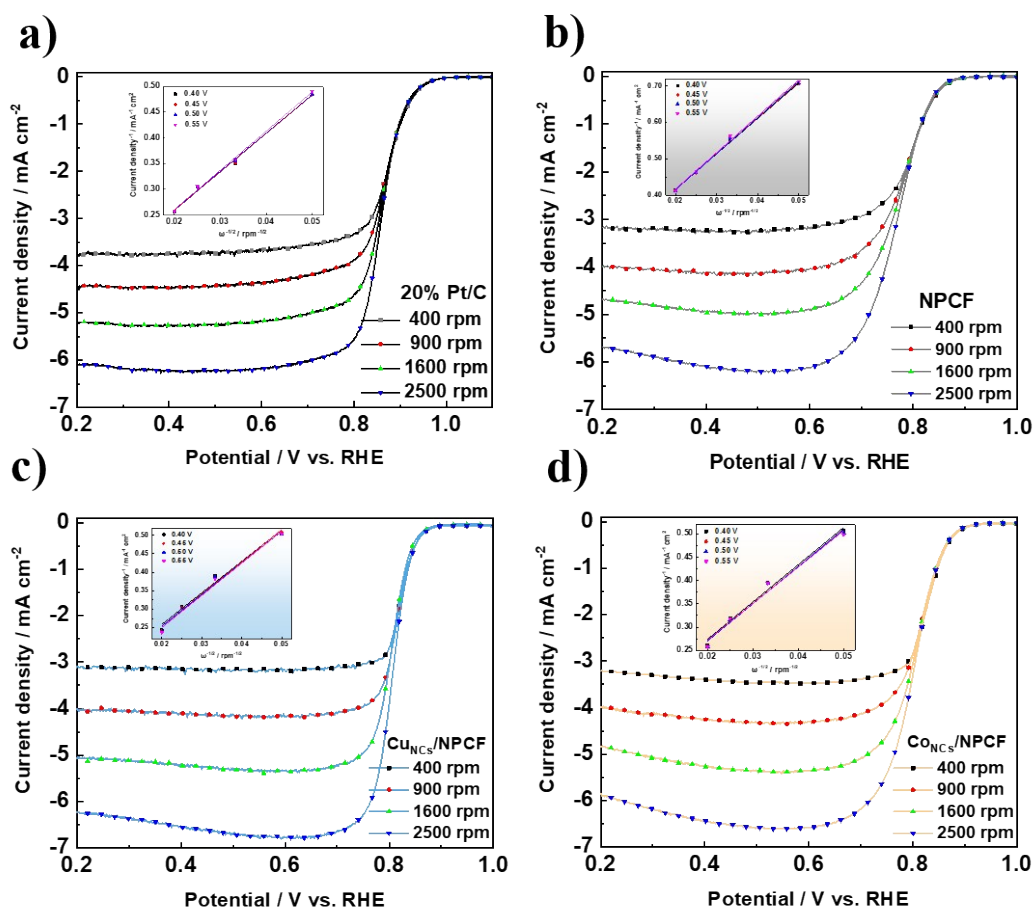


Fig. S11. LSV curves and K-L plots of (a) 20% Pt/C, (b) NPCF, (c) $Cu_{NCS}/NPCF$ and (d) $Co_{NCS}/NPCF$ samples on RDE in O_2 -saturated 0.1 M KOH solution at various rotation rates.

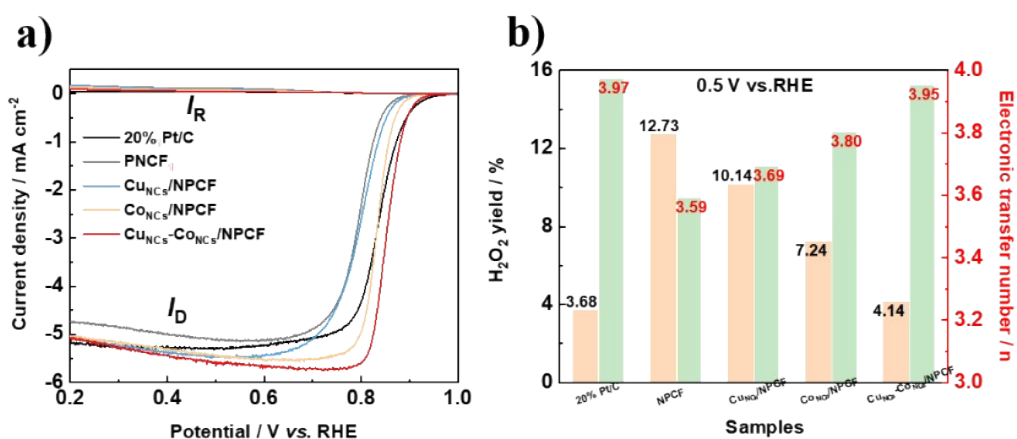


Fig. S12. (a) ORR LSV curves at 1600 rpm in an O_2 -saturated 0.10 M KOH with a scan rate of 5 $mV s^{-1}$ on RRDE, (b) H_2O_2 yield and electron transfer number plots at 0.5 V vs. RHE of 20% Pt/C, NPCF, $Cu_{NCS}/NPCF$, $Co_{NCS}/NPCF$ and $Cu_{NCS}-Co_{NCS}/NPCF$ samples.

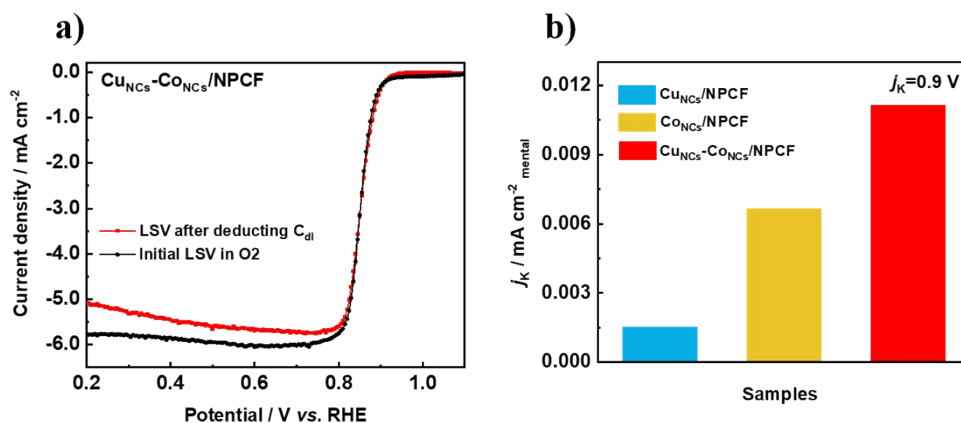


Fig. S13. (a) LSV after deducting C_{dl} and Initial LSV in O_2 of $Cu_{NCS}-Co_{NCS}/NPCF$ sample at 1600 rpm in an O_2 -saturated 0.10 M KOH with a scan rate of 5 mV s^{-1} . (b) Specific activity at 0.9 V vs. RHE for $Cu_{NCS}/NPCF$, $Co_{NCS}/NPCF$ and $Cu_{NCS}-Co_{NCS}/NPCF$ samples at the constant temperature of $30\text{ }^\circ\text{C}$.

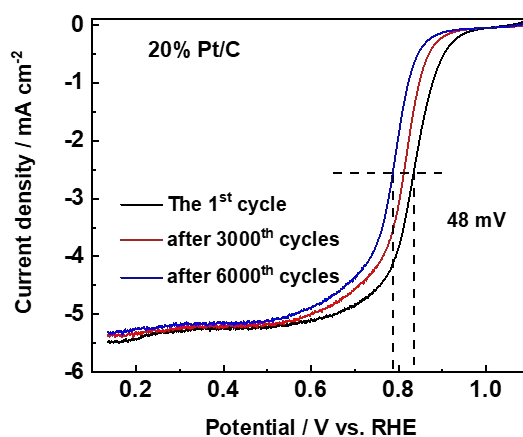


Fig. S14. LSV curves of the 1st, 3000th cycles and 6000th cycles for ORR on 20% Pt/C electrode in an O_2 -saturated 0.10 M KOH with a scan rate of 5 mV s^{-1} .

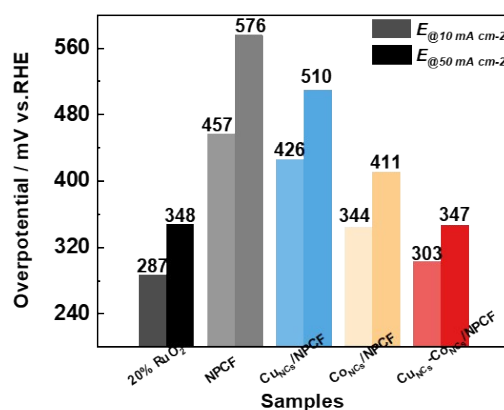


Fig. S15. Overpotential at 10 and 50 mA·cm⁻² of RuO₂/NF, NPCF/NF, Cu_{NCs}/NPCF/NF, Co_{NCs}/NPCF/NF and Cu_{NCs}-Co_{NCs}/NPCF/NF samples.

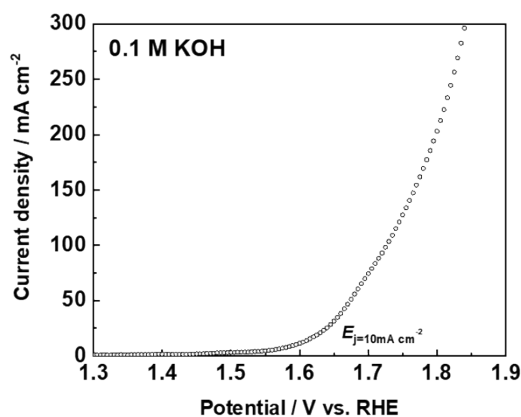


Fig. S16. OER LSV curves in 0.1 M KOH with a scan rate of 5 mV s⁻¹ of Cu_{NCs}-Co_{NCs}/NPCF sample.

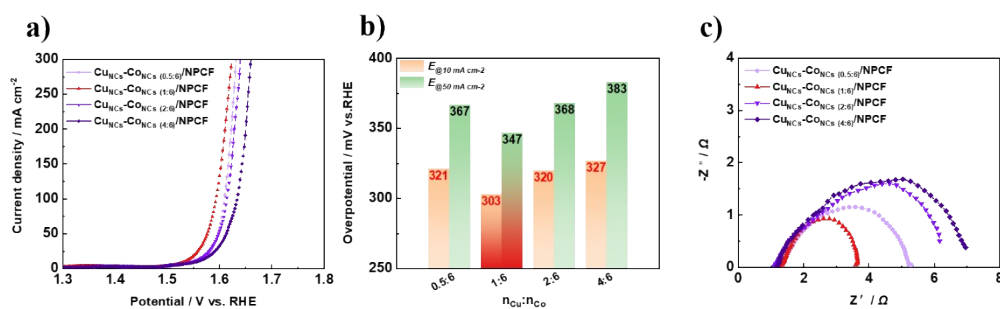


Fig. S17. (a) OER LSV curves in 1.0 M KOH with a scan rate of 5 mV s⁻¹, (b) corresponding overpotential at 10 and 50 mA·cm⁻², (c) Nyquist plots at +1.533 V vs. RHE of Cu_{NCs}-Co_{NCs} (0.5:6)/NPCF, Cu_{NCs}-Co_{NCs} (1:6)/NPCF, Cu_{NCs}-Co_{NCs} (2:6)/NPCF and Cu_{NCs}-Co_{NCs} (4:6)/NPCF samples.

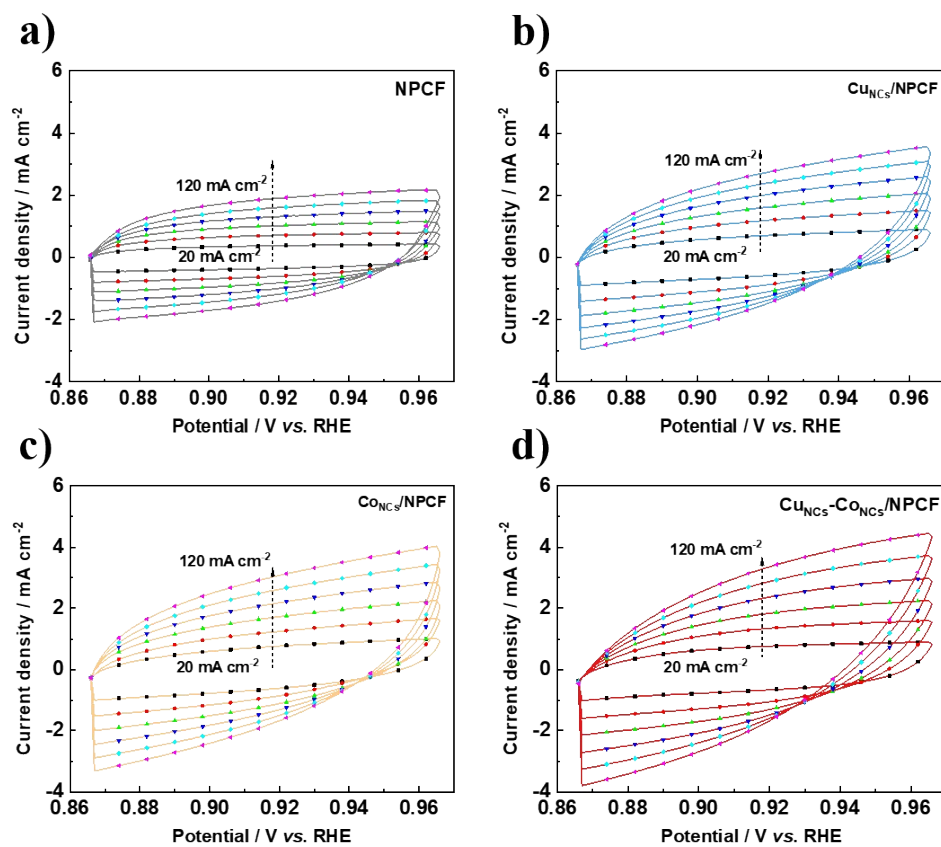


Fig. S18. CV plots with scan rates from 20 mV s^{-1} to 120 mV s^{-1} of (a) NPCF, (b) $\text{Cu}_{\text{NCs}}/\text{NPCF}$, (c) $\text{Co}_{\text{NCs}}/\text{NPCF}$ and (d) $\text{Cu}_{\text{NCs}}\text{-Co}_{\text{NCs}}/\text{NPCF}$ samples.

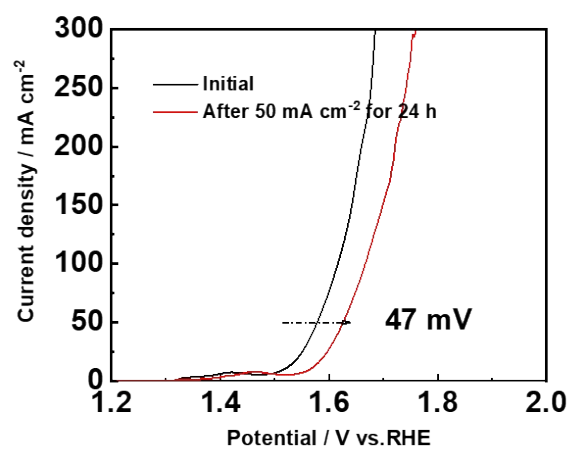


Fig. S19. LSV curves of the initial and after 24 h at 50 mA cm^{-2} for OER on RuO_2 electrode in 1.0 M KOH at a scan rate of $5 \text{ mV} \cdot \text{s}^{-1}$.

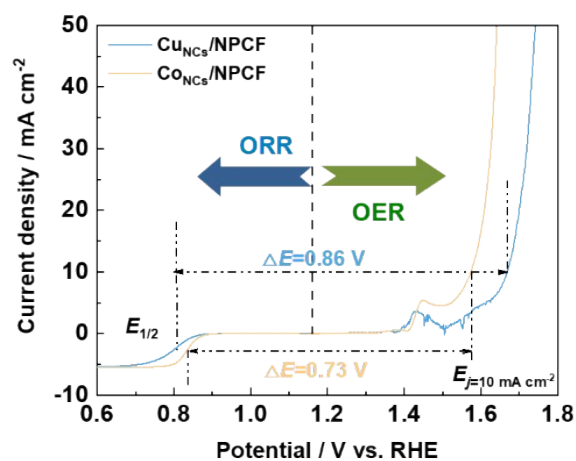


Fig. S20. The entire LSV curves for bifunctional activities within the ORR and OER potential window of Cu_{NCs}/NPCF and Cu_{NCs}/NPCF samples.

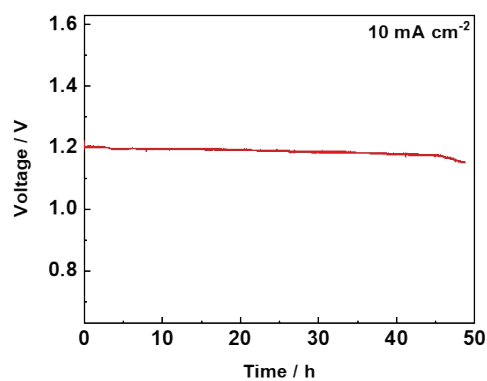


Fig. S21. Long term stability of Cu_{NCs}-Co_{NCs}/NPCF-assembled ZABs at 10 mA cm⁻².

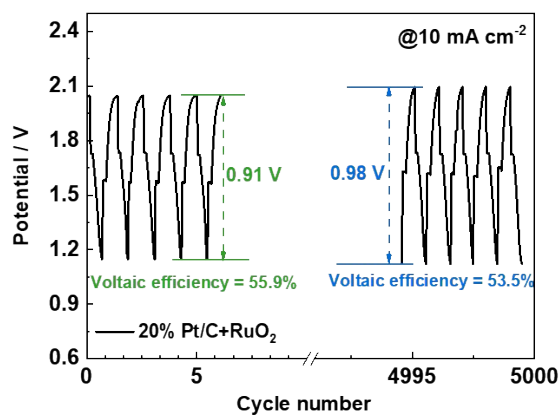


Fig. S22. Galvanostatic discharge-charge cycling profiles at 10 mA cm⁻² and corresponding voltage efficiency of the 20% Pt/C+RuO₂-assembled ZAB.

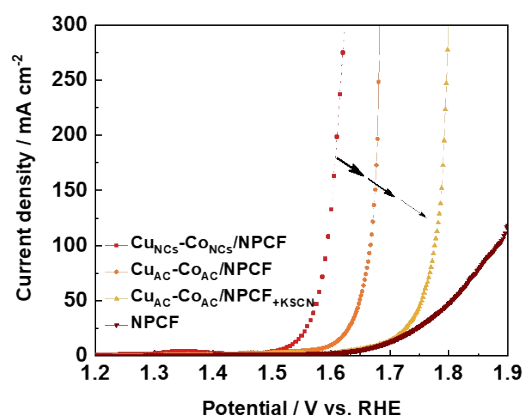


Fig. S23. OER LSV curves in 1.0 M KOH with scan rate of 5 mV s⁻¹ for Cu_{NCS}-Co_{NCS}/NPCF, Cu_{AC}-Co_{AC}/NPCF, Cu_{AC}-Co_{AC}/NPCF+KSCN and NPCF samples.

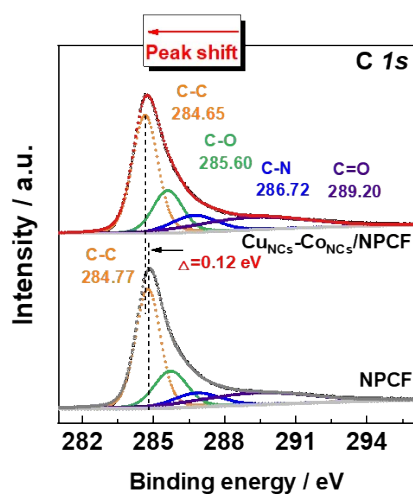


Fig. S24. High-resolution C 1s XPS spectra of NPCF and Cu_{NCS}-Co_{NCS}/NPCF samples.

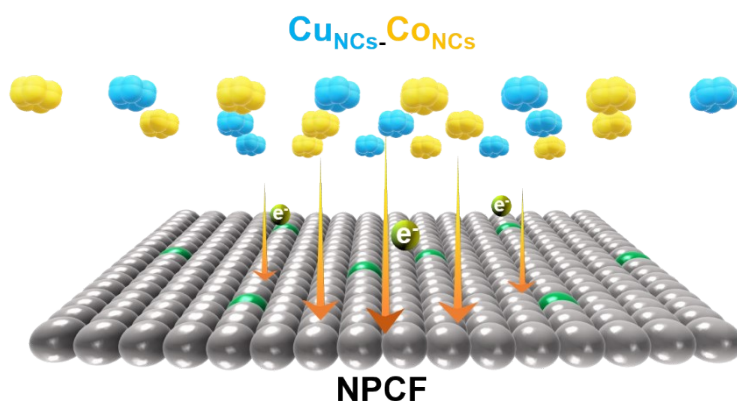


Fig. S25. The schematic diagram for the charge transfer between Cu/Co metallic phase and NPCF substrate.

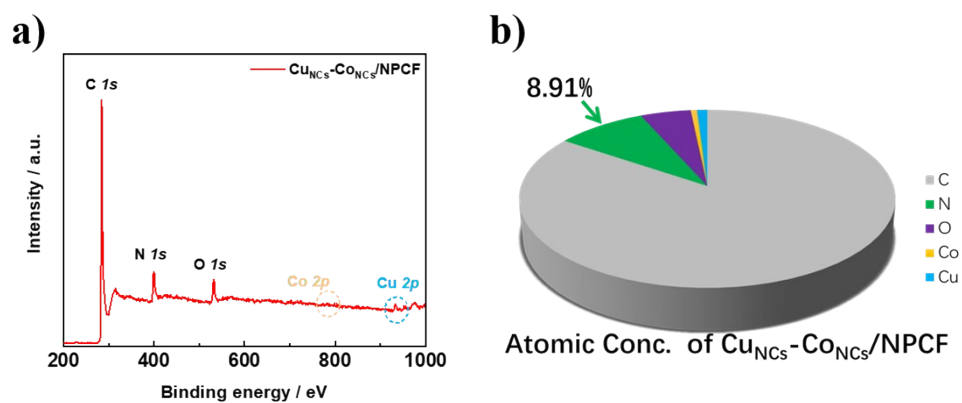


Fig. S26. (a) XPS spectrum and (b) atomic conc. of Cu_{NCs}-Co_{NCs}/NPCF sample.

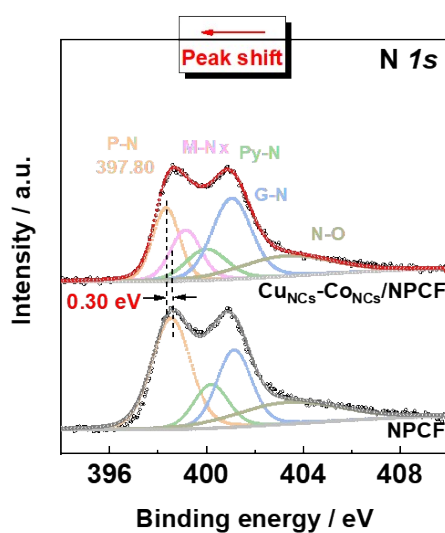


Fig.S27. High-resolution N 1s XPS spectra of NPCF and Cu_{NCs}-Co_{NCs}/NPCF samples.

Table S1. The BET surface area of the prepared Cu_{NCs}-Co_{NCs}/NPCF catalyst sample compared with the reported results in literature.

Catalysts	BET (surface area/m ² g ⁻¹)	References
Cu_{NCs}-Co_{NCs}/NPCF	493.08	This work
Co ₂ Ni ₁ LDH-GO	84.87	1
Fe-Mn ₃ O ₄ HYSNBs	120.80	2
FeCo-N-C-700	332.00	3
Fe-N-NDC-1-900	346.40	4
Co-ISAS/p-CN	380.00	5
Ni ₃ Fe/N-C sheets	447.00	6
Co/CoFe@NC	468.60	7
FeCu-DA/NC	488.80	8
Cu-N-C	512.20	9
Cu-CoNCNs	550.88	10

Table S2. The ORR performance of the prepared Cu_{NCS}-Co_{NCS}/NPCF catalyst compared with the recently reported electrocatalysts under alkaline condition.

Catalysts	Loading (mg cm ⁻²)	E_0 (V vs. RHE)	$E_{1/2}$ (V vs. RHE)	References
Cu _{NCS} -Co _{NCS} /NPCF	0.20	0.97	0.85	This work
Fe-Mn ₃ O ₄ HYSNBs	0.26	1.02	0.78	2
Fe-N-NDC-1-900	0.195	1.06	0.89	4
Co-ISAS/p-CN	-	-	0.84	5
Co/CoFe@NC	0.25	0.97	0.84	7
FeCu-DA/NC	0.5	0.96	0.86	8
Cu-N-C	0.53	-	0.87	9
FeCu _{1.0} @NC	0.380	0.89	-	11
NP-Ag ₄ Cu	0.02	0.82	-	12
Cu-SAs/N-C	0.09	-	0.90	13
FeNi/N-LCN	0.8	0.97	0.85	14
FeCo/Se-CNT	0.38	0.97	0.90	15
(Ni,Cu)-NG	0.36	-	0.84	16
FeCo/Co ₂ P@NPCF	-	0.85	0.79	17

Table S3. The OER performance of the prepared Cu_{NCS}-Co_{NCS}/NPCF catalyst compared with previously reported electrocatalysts.

Catalysts	$E_{j=10 \text{ mA cm}^{-2}}(\text{V})$	Tafel slop (mV dec^{-1})	References
Cu_{NCS}-Co_{NCS}/NPCF	1.53	74.40	This work
Fe-N-NDC-1-900	1.58	66.30	4
Co/CoFe@NC	1.54	49.00	7
FeNi/N-LCN	1.57	75.00	14
FeCo/Se-CNT	1.57	74.20	15
FeCo/Co ₂ P@NPCF	1.56	61.00	17
Fe-N/S-CNT-GR	1.60	-	18
Co/Co ₂ P@NPCNTs	1.54	71.50	19
FeS/Fe ₃ C@N-S-C-800	570	81.00	20
Cu ₉₇ P _{3-x-y} O _x N _y /NPC	1.57	69.00	21
CoNi@NCNTs/CC	1.56	64.00	22

Table S4. The ORR/OER activities of the prepared Cu_{NCs}-Co_{NCs}/NPCF catalyst compared with recently reported bifunctional electrocatalysts.

Catalysts	$E_{j=10 \text{ mA cm}^{-2}}$ (V)	$E_{1/2}$ (V vs. RHE)	ΔE (V vs. RHE)	References
Cu_{NCs}-Co_{NCs}/NPCF	1.53	0.85	0.68	This work
6-FeCo-N-C-700	1.60	0.89	0.71	3
3-Fe-N-NDC-1-900	1.58	0.89	0.69	4
12-Ni ₃ Fe/N-C	1.60	0.78	0.82	6
4-Co/CoFe@NC	1.54	0.84	0.70	7
7-FeNi/N-LCN	1.57	0.85	0.72	14
1-FeCo/Se-CNT	1.57	0.90	0.67	15
2-FeCo/Co ₂ P@NPCF	1.57	0.89	0.68	17
5-Fe-N/S-CNT-GR	1.60	0.90	0.70	18
8-CoNi@NCNTs/CC	1.56	0.83	0.73	22
10-3D Fe/N-G#4	1.62	0.85	0.77	23
13-SNC	1.67	0.78	0.89	24
11-N-Co ₃ O ₄ @NC-2	1.60	0.82	0.78	25
9-CuCo ₂ S ₄ NSs@N-CNFs	1.54	0.79	0.75	26

Table S5. Performance comparison of the Cu_{NCs}-Co_{NCs}/NPCF-assembled ZAB with those reported in literature.

Catalysts	OCP (V)	Peak power density (mW cm ⁻²)	References
Cu_{NCs}-Co_{NCs}/NPCF	1.46	135.24	This work
Fe-Mn ₃ O ₄ HYSNBs	1.40	100.00	2
Fe-N-NDC-1-900	1.48	200.00	4
Co/CoFe@NC	1.49	140.00	7
NP-Ag ₄ Cu	1.47	145.00	12
FeNi/N-LCN	1.49	162.00	14
FeCo/Se-CNT	-	155.00	15
(Ni,Cu)-NG	-	140.00	16
Fe-N/S-CNT-GR	-	123.00	18
CoNi@NCNTs/CC	1.49	114.00	22

References

1. W. Zhao, T. Liu, N. Wu, B. Zhou, Y. Yan, Y. Ye, J. Gong and S. Yang, *Science China Materials*, 2022.
2. T. Li, Y. Hu, K. Liu, J. Yin, Y. Li, G. Fu, Y. Zhang and Y. Tang, *Chemical Engineering Journal*, 2022, **427**.
3. X. Duan, S. Ren, N. Pan, M. Zhang and H. Zheng, *Journal of Materials Chemistry A*, 2020, **8**, 9355-9363.
4. Z. Jie, C. Jinwei, L. Yan, C. Yihan, L. Yingjian, Z. Chenyang, X. Yali, L. Honggang, W. Gang and W. Ruilin, *Journal of Materials Chemistry A*, 2021, DOI: 10.1039/d0ta11859a.
5. A. Han, W. Chen, S. Zhang, M. Zhang, Y. Han, J. Zhang, S. Ji, L. Zheng, Y. Wang, L. Gu, C. Chen, Q. Peng, D. Wang and Y. Li, *Advanced materials*, 2018, **30**, e1706508.
6. G. Fu, Z. Cui, Y. Chen, Y. Li, Y. Tang and J. B. Goodenough, *Advanced Energy Materials*, 2017, **7**.
7. Y. Niu, X. Teng, S. Gong, M. Xu, S. G. Sun and Z. Chen, *Nanomicro Lett*, 2021, **13**, 126.
8. C. Du, Y. Gao, H. Chen, P. Li, S. Zhu, J. Wang, Q. He and W. Chen, *Journal of Materials Chemistry A*, 2020, **8**, 16994-17001.
9. F. Li, G. F. Han, H. J. Noh, S. J. Kim, Y. Lu, H. Y. Jeong, Z. Fu and J. B. Baek, *Energy & Environmental Science*, 2018, **11**, 2263-2269.
10. S. Xie, L. Li, Y. Chen, J. Fan, Q. Li, Y. Min and Q. Xu, *ACS Applied Materials Interfaces*, 2021, **13**, 3949-3958.
11. X. Chen, R. Qin, Z. Li, S. Shan, Y. Liu and C. Yang, *Molecular Catalysis*, 2021, **500**.
12. S. Yin, Y. Shen, J. Zhang, H.-M. Yin, X.-Z. Liu and Y. Ding, *Applied Surface Science*, 2021, **545**, 149042545-149149051.
13. Y. Qu, Z. Li, W. Chen, Y. Lin, T. Yuan, Z. Yang, C. Zhao, J. Wang, C. Zhao, X. Wang, F. Zhou, Z. Zhuang, Y. Wu and Y. Li, *Nature Catalysis*, 2018, **1**, 781-786.
14. X. Li, Y. Liu, H. Chen, M. Yang, D. Yang, H. Li and Z. Lin, *Nano Lett*, 2021, **21**, 3098-3105.
15. H. Zhang, M. Zhao, H. Liu, S. Shi, Z. Wang, B. Zhang, L. Song, J. Shang, Y. Yang, C. Ma, L. Zheng, Y. Han and W. Huang, *Nano Letters*, 2021, **21**, 2255-2264.
16. Y. Cheng, H. Wu, J. Han, S. Zhong, S. Huang, S. Chu, S. Song, K. M. Reddy, X. Wang, S. Wu, X. Zhuang, I. Johnson, P. Liu and M. Chen, *Nanoscale*, 2021, **13**, 10862-10870.
17. Q. Shi, Q. Liu, Y. Ma, Z. Fang, Z. Liang, G. Shao, B. Tang, W. Yang, L. Qin and X. Fang, *Advanced Energy Materials*, 2020, **10**, 1903854-1903864.
18. W. Y. Noh, J. Mun, Y. Lee, E. M. Kim, Y. K. Kim, K. Y. Kim, H. Y. Jeong, J. H. Lee, H.-K. Song, G. Lee and J. S. Lee, *ACS Catalysis*, 2022, **12**, 7994-8006.
19. H. Yang, B. Wang, S. Kou, G. Lu and Z. Liu, *Chemical Engineering Journal*, 2021, **425**, 131589-131598.
20. X. Wang, J. Sunarso, Q. Lu, Z. Zhou, J. Dai, D. Guan, W. Zhou and Z. Shao, *Advanced Energy Materials*, 2019, **10**, 1903271-1903280.
21. B. Yuan, G. Nam, P. Li, S. Wang, H. Jang, T. Wei, Q. Qin, X. Liu and J. Cho, *Journal of Power Sources*, 2019, **421**, 109-115.
22. W. Tian, J. Ren and Z. Yuan, *Applied Catalysis B: Environmental*, 2022, **317**, 121764-121776.
23. C. Wang, Z. Li, L. Wang, X. Niu and S. Wang, *ACS Sustainable Chemistry & Engineering*, 2019, **7**, 13873-13885.
24. S. Y. Yibo Guo, Longxue Gao, An Chen, Menggai Jiao, Huijuan Cui, Zhen Zhou, *J. Mater.*

Chem. A, 2020, **8**, 4386-4395

25. Z. Wang, W. Xu, X. Chen, Y. Peng, Y. Song, C. Lv, H. Liu, J. Sun, D. Yuan, X. Li, X. Guo, D. Yang and L. Zhang, *Advanced Functional Materials*, 2019, 1902875-1902885.
26. Z. Pan, H. Chen, J. Yang, Y. Ma, Q. Zhang, Z. Kou, X. Ding, Y. Pang, L. Zhang, Q. Gu, C. Yan and J. Wang, *Advanced Science*, 2019, **6**, 1900628-1900637.